RSC Advances

PAPER

View Article Online
View Journal | View Issue

Open Access Article. Published on 12 September 2022. Downloaded on 2/12/2026 3:28:12 PM.
This article is licensed under a Creative Commons Attribution-NonCommercial 3.0 Unported Licence.

Check for updates

Cite this: *RSC Adv.*, 2022, **12**, 25833

Enhancing mechanism of arsenic(III) adsorption by MnO_2-loaded calcined MgFe layered double hydroxide†

Mingqi Xie,[ab] Xiangping Luo,[ab] Chongmin Liu,[*ab] Shaohong You,[ab] Saeed Rad,[ab] Huijun He,[ab] Yongxiang Huang[ab] and Zhihong Tu[abc]

Received 2nd August 2022
Accepted 31st August 2022

DOI: 10.1039/d2ra04805a

rsc.li/rsc-advances

The use of MnO_2/MgFe-layered double hydroxide (MnO_2/MgFe-LDH) and MnO_2/MgFe-layered double oxide (MnO_2/MgFe-LDO$_{400\ ^\circ C}$) for arsenic immobilization from the aqueous medium is the subject of this research. Fourier transform infrared spectroscopy, X-ray diffraction, X-ray photoelectron spectroscopy, scanning electron microscopy, and transmission electron microscopy were used to characterise MnO_2/MgFe-LDH and MnO_2/MgFe-LDO$_{400\ ^\circ C}$. Based on our developed method, MnO_2 was spread on the clay composites' surfaces in the form of a chemical bond. The clay composite exhibited a good adsorption effect on arsenic. The experimental findings fit the pseudo-second-order model well, indicating that the chemisorption mechanism played a significant role in the adsorption process. Furthermore, the Freundlich model suited the adsorption isotherm data of all adsorbents well. The recycling experiment showed that MnO_2/MgFe-LDH and MnO_2/MgFe-LDO$_{400\ ^\circ C}$ exhibited good stability and reusability. In summary, MnO_2/MgFe-LDH and MnO_2/MgFe-LDO$_{400\ ^\circ C}$ are promising for developing processes for efficient control of the pollutant arsenic.

1. Introduction

As one of the most dangerous elements in wastewater effluents, arsenic is an extremely toxic metal described as a potent class-one non-threshold carcinogen.[1] Arsenic poisoning can harm plant growth, development, and metabolism, resulting in yield loss. In addition, arsenic levels in the human body rise as a result of drinking arsenic-contaminated water or consuming foods with high arsenic contents. Increased arsenic levels are linked to various acute and chronic human health issues, including malignancies and adverse effects on the cardiovascular, neurological, hematological, renal, reproductive, and respiratory systems.[2,3] The World Health Organization has set the maximum safe limit of arsenic in drinking water to 10 μg L^{-1} because of its extreme toxicity and carcinogenicity. However, several areas worldwide, including China, still suffer from the threat of arsenic contamination.[4,5] Approximately 20 million Chinese people are possibly exposed to drinking water contaminated with arsenic. Therefore, there is an urgent need to explore environmentally friendly ways to remove arsenic from the aquatic environment.

Extensive studies have been conducted on the treatment of arsenic using biological methods,[6] coagulation,[7] adsorption,[8] and the reverse osmosis method.[9] Among there, adsorption is one of the most promising technologies for arsenic removal from aqueous solutions because of its simple operation and broad applicability. In addition, the adsorption method can achieve a high removal efficiency and recover arsenic from aqueous solutions with different arsenic concentrations over a wide range of pH values. Various materials for arsenic removal are continuously being evaluated by researchers worldwide, including activated carbon,[10] biochar-based sorbents,[11] organic polymers,[12] and Al_2O_3.[13] However, the reported adsorbents could adsorb arsenate (As(V)) more easily, but experienced difficulty attaching arsenite (As(III)). Arsenic occurs in two main states in the natural aquatic environment: trivalent (As(III)) and pentavalent (As(V)). The toxicity of As(III) is 20–60 times higher than that of As(V).[14] In addition, compared to As(V), As(III) is more difficult to be removed from water than As(V), is easier to transfer in the environment, and has a stronger ability to enter biological cells under neutral and acidic conditions.[15] Therefore, we focused on evaluating an efficient adsorption material for As(III) contamination.

Manganese is one of the most widely distributed elements in the environment, and manganese oxides showed a high affinity to various pollutants.[16] Among these Mn-oxides, manganese dioxide (MnO_2) is non-toxic and has extensive sources, and has

[a]College of Environmental Science and Engineering, Guilin University of Technology, Guilin 541004, China. E-mail: chongmin@glut.edu.cn

[b]Guangxi Key Laboratory of Theory & Technology for Environmental Pollution Control, Guilin University of Technology, Guilin 541004, China

[c]CAS Key Laboratory of Mineralogy and Metallogeny, Guangzhou Institute of Geochemistry, Chinese Academy of Sciences, Guangzhou 510640, China

† Electronic supplementary information (ESI) available. See https://doi.org/10.1039/d2ra04805a

© 2022 The Author(s). Published by the Royal Society of Chemistry

Open Access Article. Published on 12 September 2022. Downloaded on 2/12/2026 3:28:12 PM.
This article is licensed under a Creative Commons Attribution-NonCommercial 3.0 Unported Licence.

been applied in the removal of various pollutants from the aquatic environment.[17] Owning to its oxidation, MnO_2 showed excellent superiority as an adsorbent for As(III) removal. Wei *et al.* reported that MnO_2 could remove As(III) by absorption and oxidisation.[18] Jian *et al.* used β-MnO_2 composite materials to adsorb arsenic(III), indicating that MnO_2 oxidises As(III) to As(V), resulting in an easier removal of As(III) from water.[19] However, this material is difficult to crystallise during synthesis, undergoes reduction easily, and releases manganese ions during the process of As(III) oxidation. Some precursor studies have proven that loading on a suitable carrier, to form the compound materials could be an efficient way to overcome the disadvantages of MnO_2 and improve its application.[20,21]

Layered double hydroxides (LDHs), known as anionic clays or hydrotalcites, are a kind of materials that have attracted attention worldwide owing to their low cost, high anion exchange capacity, large specific surface area, and excellent interlayer intercalation. Moreover, their calcined products, namely layered double oxides (LDOs), have many advantages, including uniform dispersion, excellent thermal stability, huge specific surface areas, and synergistic action between elements.[22] Benefiting from excellent characteristics, these two types of materials have been extensively used as precursors for catalyzers[23] and absorbents.[24] Dai *et al.* developed a novel two-dimensional magnetic NiFe LDH nanosheet grown on diatomite with superior adsorption performance for anionic, cationic dyes, As(III), and As(V) from wastewater.[25] Long *et al.* synthesized polyaniline/Mg–Al layered double oxides which the composites showed highly efficient removal of hexavalent chromium from aqueous solution. Furthermore, "memory effect" of LDOs performed favorable ability for arsenic removal.[26] The research of Lv *et al.* revealed that controlling the calcination temperature to 500 °C could enhance the As(V) adsorption capacity of NiAL-LDO composite.[27] Also Mubarak *et al.* reported that the MgFe-LDO hollow nanospheres showed high adsorption effectiveness for As(V).[28] Thus there are reasons to believe the combination of MnO_2 and LDO to form composites can provide potential adsorbents to enhance As(III) oxidation and adsorption activity through the synergistic effects between MnO_2 and LDO. However, to our knowledge, little research has been done in this aspect. Meanwhile, the related arsenic removal mechanism is worth exploring.

In this study, MnO_2-doped MgFe LDH and LDO were successfully synthesised to efficiently remove arsenate from aqueous solutions. This research aimed to investigate the adsorption behaviour and preliminary mechanism of clay composites (MnO_2/MgFe-LDH, MnO_2/MgFe-$LDO_{400\ °C}$) for As(III) removal.

2. Materials and methods

2.1 Chemicals

The chemicals $Mg(NO_3)_2 \cdot 6H_2O$, $Fe(NO_3)_3 \cdot 9H_2O$, $KMnO_4$, $MnCl_2 \cdot 4H_2O$, $NaAsO_2$, NaOH, Na_2CO_3, NaCl, HCl, H_2SO_4, H_2SO_4, and HNO_3 were purchased from Xilong Scientific Co., Ltd. The chemical reagents used in this study were of analytical grade, and solutions were prepared using deionised (DI) water.

2.2 Material synthesis methods

The co-precipitation approach was used to prepare MnO_2/MgFe-LDH. To prepare the mixed aqueous solution, 4.615 g of $Mg(NO_3)_2 \cdot 6H_2O$ and 2.424 g of $Fe(NO_3)_3 \cdot 9H_2O$ were dissolved in 300 mL of DI water. Under vigorous stirring, NaOH was slowly added dropwise to the mixed solution. The pH of the reaction solution was maintained at 11 ± 0.5 by controlling the lowering speed of the NaOH solution. After 48 h of ageing at 60 °C, the $KMnO_4$ and $MnCl_2 \cdot 4H_2O$ were carefully added, followed by 4 h of stirring at 30 °C. After ageing for 12 h, the slurry was centrifuged and rinsed numerous times with DI water until the supernatant was neutral. The MnO_2/MgFe-LDH was then dried at 70 °C, and crushed into a powder. Finally, a portion of the MnO_2/MgFe-LDH powder was calcined at 400 °C for 5 h in a tube furnace to produce MnO_2/MgFe-$LDO_{400\ °C}$.

2.3 Characterisation and analysis

The surface physical morphology and microstructure of the clay composites were determined by a scanning electron microscopy (SEM). The transmission electron microscopy (TEM) was employed for microstructural and compositional analyses of the clay composites. The specific surface areas were determined using the Brunauer–Emmett–Teller (BET) method. A Nano ZS 90 type nanoparticle size and zeta potential analyser was used to analyse and test the zeta potential of the materials. X-ray diffraction (XRD) patterns were obtained using an X'Pert 3 Powder diffractometer (PNAlytical, Holland) with copper K_α radiation (λ = 1.54059 Å). Fourier transform infrared spectroscopy (FT-IR) was used to observe the structural changes in the particle surface. The surface elements species were analysed using X-ray photoelectron spectroscopy (XPS).

2.4 Adsorption experiments

2.4.1 Material selection. Briefly, 30 mg of the materials were added to 30 mL of 50 mg L^{-1} As(III). After the reaction, residual As(III) was measured using inductively coupled plasma emission spectrometry (ICP-OES) concentration.

2.4.2 Effect of pH on adsorption. The effect of pH on the adsorption of As(III) by the adsorbents was studied in the pH range 2 to 12. In the solution containing 50 mg L^{-1} As(III), the adsorbent concentration (MnO_2/MgFe-LDH and MnO_2/MgFe-$LDO_{400\ °C}$) was maintained at 1.0 g L^{-1}. The pH was adjusted with 0.1 M HCl or NaOH. To reach the adsorption equilibrium, the adsorbent-desorbent system oscillated in a constant-temperature oscillator at a speed of 160 rpm. The solution was removed and passed through a 0.45 μm aqueous filter membrane, and the residual As(III) concentration was measured using ICP-OES.

2.4.3 Kinetic adsorption. Briefly, 30 mg of MnO_2/MgFe-LDH and MnO_2/MgFe-$LDO_{400°C}$ were each into 30 mL of 30, 40 and 50 mg L^{-1} As(III) solutions,. The suspensions were placed in a shaker and samples were withdrawn at 5; 10; 30; 60; 120; 240; 360; 540; 720; 1080; 1440; 1800; 2160; 2520; 2880; 3240;

 © 2022 The Author(s). Published by the Royal Society of Chemistry

Open Access Article. Published on 12 September 2022. Downloaded on 2/12/2026 3:28:12 PM.
This article is licensed under a Creative Commons Attribution-NonCommercial 3.0 Unported Licence.

3600; and 3960 min. Then, suspensions were filtered through 0.45 μm syringe filters, and As(III) concentrations were measured using an ICP-OES (Optima 7000 DV,USA). Three replicates were performed for each contact time point. The pseudo-first-order (eqn (1)) and pseudo-second-order (eqn (2)),[29] equations were used for data modelling.

$$\ln(Q_e - Q_t) = \ln Q_e - K_1 t \quad (1)$$

$$\frac{t}{q_t} = \frac{1}{k_2 q_e^2} + \frac{t}{q_e} \quad (2)$$

where q_e (mg g^{-1}) and q_t (mg g^{-1}) are the amounts of arsenic adsorbed by the clay composites at equilibrium and at time t (min), respectively, and k_1, and k_2 are the rate constants of the pseudo first-order, and pseudo second-order kinetic equations, respectively.

2.4.4 Isotherm adsorption. Here, 30 mg each of MnO_2/MgFe-LDH and MnO_2/MgFe-LDO $_{400\ °C}$ composite materials were placed into individual 50 mL centrifuge tubes weighted and then added 30 mL of the initial concentration of 1, 2, 5, 10, 20, 30, 40, 50, 60, 80, and 100 mg L^{-1} As(III) solution was added to each individual tubes. The solutions were placed in a shaker at 25 °C, 35 °C, and 45 °C till it reached equilibrium. After collecting the supernatant was taken, the solution was measured after passing through a 0.45 μm water filter membrane residual As(III) concentrations. Langmuir (eqn (3)) and Freundlich (eqn (4)) adsorption isotherm models were sued to evaluate the adsorption capacity at different temperatures.[30] The equations are expressed as follows.

$$q = \frac{q_m \times k_L \times C_e}{1 + k_L \times C_e} \quad (3)$$

$$q = K_L \times C_e^{\frac{1}{n}} \quad (4)$$

where q (mg g^{-1}) is the adsorption capacity of the target pollutants in the adsorption equilibrium, q_m (mg g^{-1}) is the adsorption capacity of the mixture for target pollutants, C_e (mg L^{-1}) is the equilibrium concentration of As(III) on the clay composites, n is a characteristic constant related to the adsorption strength or favourable adsorption degree, and lastly, K_L (L mg^{-1}) and K_F (mg g^{-1}) are the Langmuir and Freundlich constants, respectively. The adsorption type can be preliminarily determined according to K_L. The K_L value decreased as the temperature increased, indicating that the adsorption process was exothermic and involved physical adsorption. Otherwise, it is an endothermic process, that is, a chemical adsorption process.

2.4.5 Desorption. Following the adsorption of As(III) by MnO_2/MgFe-LDH and MnO_2/MgFe-LDO$_{400°C}$ composite materials, 0.1 mol L^{-1} NaOH solutions were utilised as desorption solutions, which were soaked for 8 h. If the As(III) concentration in the final two desorption solutions remained below 5%, desorption was considered complete. After the desorption is completed, the substance was neutralized with ultrapure water before being used and placed in a box for drying before reuse.

3. Results and discussion

3.1 Selection of materials

Through a series of adsorption experiments, the materials of MnO_2/MgFe-LDO$_{400\ °C}$ exhibited the best adsorption performance, whereas MnO_2 had the lowest arsenic adsorption capacity. Among the LDH materials, MnO_2/MgFe-LDH displayed a slightly better adsorption capacity compared with that of MgFe-LDH (Fig. 1), with an initial arsenic concentration of 50 mg L^{-1}. Therefore, modification by calcination for MnO_2/MgFe-LDH at the temperatures of 400 °C, 500 °C, and 600 °C was carried out to improve the adsorption of As(III). The results showed that the adsorption capacity of As(III) by MnO_2/MgFe-LDO$_{400\ °C}$ reaches 35.93 mg g^{-1}, which is greater than that of MnO_2/MgFe-LDO$_{500\ °C}$ (30.09 mg g^{-1}) and MnO_2/MgFe-LDO$_{600\ °C}$ (20.82 mg g^{-1}). These phenomena can be illustrated by the irreversible oxide formation and elimination of the "memory effect" in the structure of LDH at high calcination temperatures.[27] Consequently, MnO_2/MgFe-LDO$_{400\ °C}$ presents the best removal performance for As(III) among the selected calcination temperatures.

3.2 Structure characterization

The structures of the clay composites were studied using XRD. The XRD spectrum of MgFe-LDH revealed a succession of peaks 2 = 11.341°, 22.783°, 34.142°, 38.542° and 59.388°, which correspond to (003), (006), (012), (015), and (110) of the hydrotalcite-like structure.[31] As shown in Fig. 2(a), diffraction peaks with hydrotalcite structures were also visible in the MnO_2/MgFe-LDH spectra. Furthermore, the characteristic MnO_2 peaks occurred at $2\theta = 12.183°$ (002) and 18.618° (101), indicating that the loading of MnO_2 did not disrupt the hydrotalcite structure and that the MnO_2/MgFe-LDH composite material was successfully produced. The XRD pattern of MnO_2/MgFe-LDO$_{400\ °C}$ revealed the obvious absence of several diffraction peaks, indicating that the material lost some interlayer molecules and anions, such as water molecules and CO_3^{2-}, and the layered

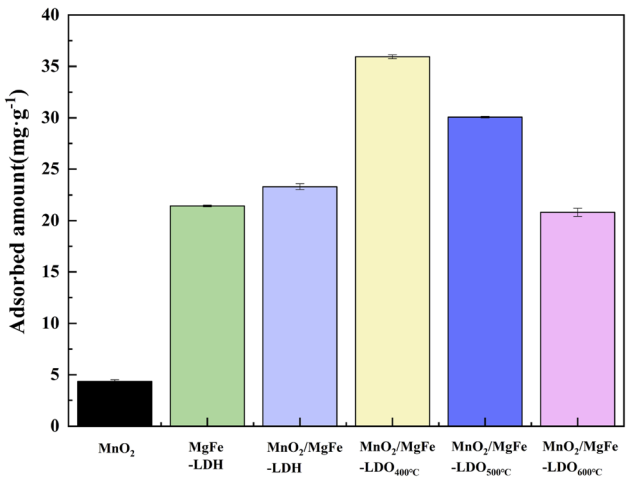

Fig. 1 Comparison of arsenic adsorption capacities of materials.

Open Access Article. Published on 12 September 2022. Downloaded on 2/12/2026 3:28:12 PM.
This article is licensed under a Creative Commons Attribution-NonCommercial 3.0 Unported Licence.

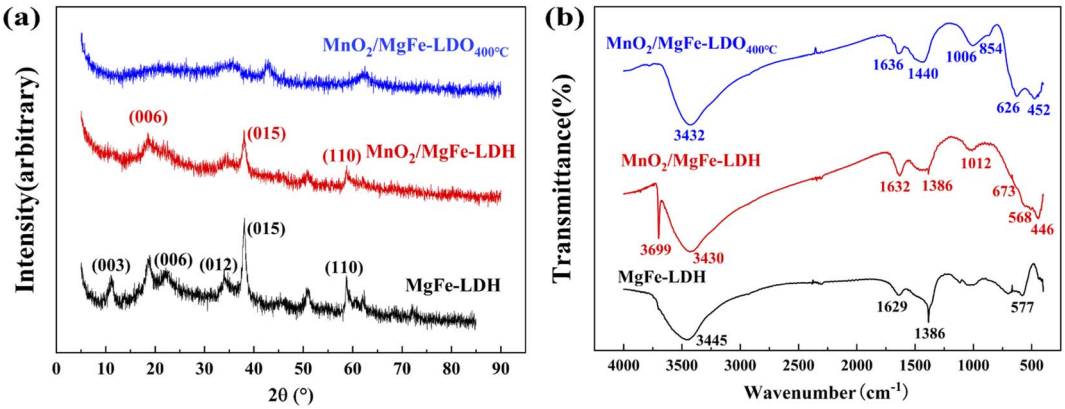

Fig. 2 (a) XRD spectra of MgFe-LDH, MnO_2/MgFe-LDH and MnO_2/MgFe-$LDO_{400\ ^\circ C}$. (b) FT-IR of MgFe-LDH, MnO_2/MgFe-LDH and MnO_2/MgFe-$LDO_{400\ ^\circ C}$.

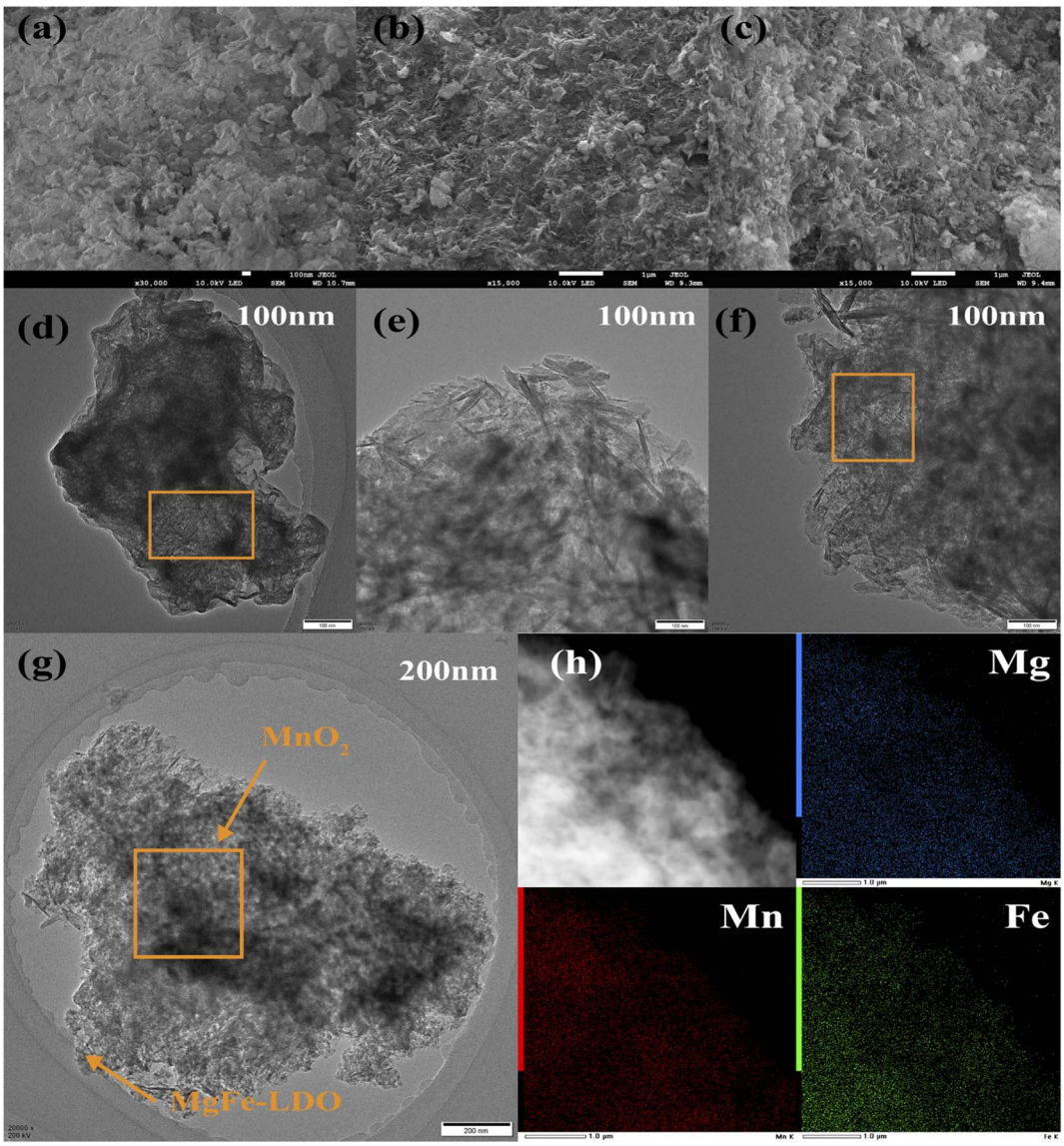

Fig. 3 (a) SEM of MgFe-LDH, (b) MnO_2/MgFe-LDH and (c) MnO_2/MgFe-$LDO_{400\ ^\circ C}$. (d) TEM image of MnO_2. (e) TEM image of MgFe-LDH, (f) TEM image of MnO_2/MgFe-LDH, (g) TEM image of MnO_2/MgFe-$LDO_{400\ ^\circ C}$, and (h) mapping of MnO_2/MgFe-LDH.

 © 2022 The Author(s). Published by the Royal Society of Chemistry

Open Access Article. Published on 12 September 2022. Downloaded on 2/12/2026 3:28:12 PM.
This article is licensed under a Creative Commons Attribution-NonCommercial 3.0 Unported Licence.

Table 1 BET characterization of samples

Sample	S_{BET}/(m^2 g^{-1})	V_{total}/(cm^2 g^{-1})	D_{BET}/nm
MgFe-LDH	154.005	0.390	10.135
MnO_2/MgFe-LDH	226.794	0.388	6.841
MnO_2/MgFe-LDH$O_{400\ °C}$	153.455	0.589	15.349

structure was disrupted, resulting in a magnesium-iron mixed metal oxide.

The FT-IR spectra are shown in Fig. 2(b). The three materials displayed prominent absorption peaks between 3400–3500 cm^{-1}, which were assigned with the O–H bending vibration peak of the interlayer water molecules and the stretching vibration of O–H on the laminate.[32] From the spectral point of view, the absorption peak of approximately 1630 cm^{-1} corresponded to the O–H vibration peak in crystallisation water.[33] The absorption peaks in the low-frequency region (less than 1000 cm^{-1}) are caused by O-M or O-M-O (M = Mg, Fe, Mn) bending vibrations.[34,35] The absorption peak in the spectra of MgFe-LDH and MnO_2/MgFe-LDH was induced by the interlayer CO_3^{2-} ion asymmetric tensile vibration at 1386 cm^{-1}. The absorption peak at 3699 cm^{-1} in the MnO_2/MgFe-LDH spectrum corresponded to the hydroxyl vibration on the sample surface, where the calcined MnO_2/MgFe-LDH material did not show an O–H peak at 3699 cm^{-1}. In addition, at 1386 cm^{-1}, CO_3^{2-} ions did not cause a vibration peak, but a new absorption peak caused by the vibration of HCO_3^- ions appeared at 1440 cm^{-1}, indicating that water loss and dehydroxylation during the calcination process, and due to decomposition, CO_3^{2-} transformed to HCO_3^-.[36] In addition, the absorption peak at 1012 cm^{-1} in the MnO_2/MgFe-LDH spectrum should be the C–O vibration in C–O-M (M = Mg, Fe, Mn), which appears at approximately 1006 cm^{-1} after calcination, indicating that MnO_2 is chemically bonded the way is loaded to LDH.[37]

The micromorphologies of three materials were studied using SEM, and the results for MgFe-LDH, MnO_2/MgFe-LDH, and MnO_2/MgFe-LDO$_{400\ °C}$ are presented in Fig. 3(a–c). The MgFe-LDH material has a plate-like structure with rough flake fragments on its surface, a typical anionic clay structure. The rough and uneven surface of the MnO_2/MgFe-LDH, with layered and scaly particles, improved the specific surface area and void ratio. The MnO_2/MgFe-LDO$_{400\ °C}$ surface had crumbled, leaving uneven shards. Many adsorption sites were found on this rough, uneven surface.

TEM was used to explore the microstructures of the materials. As displayed by the TEM image in Fig. 3(d), MnO_2 has a certain thickness, and it is clear that its surface is not perfectly smooth. MgFe LDH had sheet-like shape, composed of thin nano-scale curved platelets (Fig. 3(e)). We can see MnO_2/MgFe-LDH (Fig. 3(f)) and MnO_2/MgFe-LDO$_{400\ °C}$ (Fig. 3(g)) composites, their surface showed a morphology similar to that of MnO_2, element mapping of MnO_2/MgFe-LDH (Fig. 3(h)) indicated that the elements of Mg, Fe, and Mn were distributed uniformly in the structure. The Mn–K signal is attributed to the loading of MnO_2, which showed that MnO_2 binds to MgFe-LDH uniformly. Combined with XRD, manganese oxide was successfully loaded on MgFe-LDH.

According to BET results in Table 1, the specific surface area of MgFe-LDH after loaded MnO_2 is significantly larger than that of MgFe-LDH. While calcination could can result in the reduction of specific surface area of MnO_2/MgFe-LDH.

3.3 Effect of pH on adsorption

The pH of the materials has a significant impact on their adsorption process. The adsorption capacity of MnO_2/MgFe-LDH for As(III) diminished when the pH value increased, as illustrated in Fig. 4(a). This phenomenon can be explained by the electrostatic repulsion between As(III) and the MnO_2/MgFe-LDH. At a pH lower than 9, As(III) exists in the solution in the form of H_3AsO_3.[38] The surface of MnO_2/MgFe-LDH becomes negatively charged as the pH rises(Fig. 4(b)), and the H_3AsO_3 in the solution dissociates into $H_2AsO_3^-$, $HAsO_3^{2-}$, and AsO_3^{3-}.[39] The adsorption capacity of MnO_2/MgFe-LDO$_{400°C}$ for As(III) improves with increasing pH, and is superior to that of MnO_2/MgFe-LDH in the pH range of 3–12. Arsenic generates Fe–O–As, Mn–O–As, and other complexes with the surface metal of the material because the metal active sites of LDO are relatively uniformly spread and have a large specific surface area. When the pH value was high, As(III) anions were incorporated into the interlayer structure due to the "memory effect" of the LDO material.

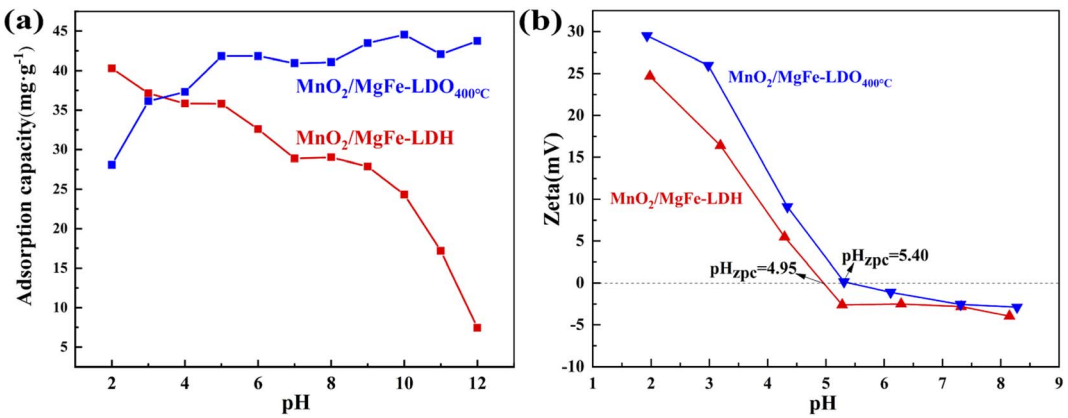

Fig. 4 (a) Effect of initial pH on the adsorption of arsenic, (b) pH-zeta of MnO_2/MgFe-LDH and MnO_2/MgFe-LDO$_{400\ °C}$ composites.

Open Access Article. Published on 12 September 2022. Downloaded on 2/12/2026 3:28:12 PM.
This article is licensed under a Creative Commons Attribution-NonCommercial 3.0 Unported Licence.

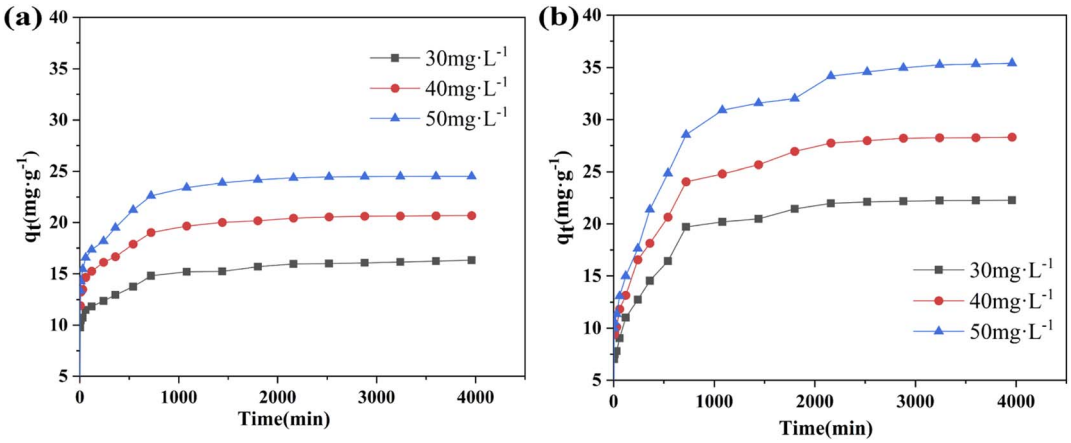

Fig. 5 The As(III) adsorption kinetics with (a) MnO_2/MgFe-LDH and (b) MnO_2/MgFe-LDO$_{400\ °C}$.

3.4 Adsorption kinetic

As shown in Fig. 5, the adsorption kinetics of the As(III) solutions showed that the amount of As(III) adsorbed increased with increasing of As(III) concentration. The MnO_2/MgFe-LDO$_{400\ °C}$ adsorption capacity increased with time and gradually tended to equilibrium. The equilibrium times were 2,520, 2,880, and 3240 minutes for the initial As(III) concentration of 30, 40, and 50 mg L^{-1}, respectively. Meanwhile, the adsorption effect of MnO_2/MgFe-LDO$_{400\ °C}$ was more significant than that of MnO_2/MgFe-LDH. The MnO_2/MgFe-LDH adsorption capacity increased with time and gradually reached equilibrium, and the equilibrium times were 1,800, 2,160, and 2520 minutes for the initial As(III) concentrations at 30, 40, and 50 mg L^{-1}, respectively.

Two kinetic models of pseudo-first-order and pseudo-second-order equations were used to investigate the adsorption behavior of MnO_2/MgFe-LDH and MnO_2/MgFe-LDO$_{400\ °C}$ on As(III) during the adsorption process. The fitted results are shown in Fig. S1,† and the relevant parameters for each kinetic model are listed in Table 2. The pseudo-second-order model was more suitable than pseudo-first-order model for fitting the experimental data of MnO_2/MgFe-LDH and MnO_2/MgFe-LDO$_{400\ °C}$ at the initial concentrations of 30, 40, and 50 mg L^{-1} As(III), where the correlation coefficients (R^2) were >0.999 and >0.996, respectively. The results showed that the adsorption of As(III) by the two composite materials was a chemical adsorption process.

3.5 Adsorption isotherm

Langmuir and Freundlich adsorption isotherm models were used to fit the adsorption behaviours of MnO_2/MgFe-LDH and MnO_2/MgFe-LDO$_{400\ °C}$ composites under different initial As(III) concentrations. The results and related parameters are presented in Fig. S2† and Table 3, respectively. Better fitting data for As(III) adsorption on the two composite materials were obtained using the Freundlich isotherm model. The adsorption capacity of the material for As(III) increased with the increasing of temperature, indicating that the adsorption process is an endothermic process. When the temperature increased, the movement of solute molecules in the system accelerates, and the mass transfer rate and diffusion coefficient increase, thereby increasing the adsorption capacity.[40]

For MnO_2/MgFe-LDH and MnO_2/MgFe-LDO$_{400\ °C}$, under the optimal experimental conditions, the maximum adsorption capacity of As(III) reached 53.8 mg L^{-1} and 51.0 mg L^{-1}, respectively (Table 3). Compared with the maximum adsorption capacities of various materials in the Table 4, MnO_2/MgFe-LDH and MnO_2/MgFe-LDO$_{400\ °C}$ present good advantages in arsenic removal.

3.6 Regeneration and reuse

Six solutions of NaOH, Na_2CO_3, NaCl, HCl, HNO_3, and H_2SO_4 with an initial concentration of 0.1 mol L^{-1} were selected as desorbents to explore the recycling performance of the material on As(III). The

Table 2 Kinetic parameters for As(III) adsorption

		Pseudo-first-order			Pseudo-second-order		
Materials	C_0 (mg L^{-1})	Q_e(mg g^{-1})	K_1	R^2	Q_e(mg g^{-1})	K_2	R^2
MnO_2/MgFe-LDH	30	5.05	4.8389×10^{-4}	0.9815	16.40	1.079×10^{-3}	0.9994
	40	7.20	7.2183×10^{-4}	0.9937	20.89	1.001×10^{-3}	0.9996
	50	10.21	8.8669×10^{-4}	0.9946	24.85	8.045×10^{-4}	0.9996
MnO_2/MgFe-LDO$_{400\ °C}$	30	15.15	7.9165×10^{-4}	0.9900	22.94	3.676×10^{-4}	0.9982
	40	19.47	7.3657×10^{-4}	0.9875	29.16	2.701×10^{-4}	0.9979
	50	25.78	6.4443×10^{-4}	0.9798	36.58	1.727×10^{-4}	0.9967

 © 2022 The Author(s). Published by the Royal Society of Chemistry

Open Access Article. Published on 12 September 2022. Downloaded on 2/12/2026 3:28:12 PM.
This article is licensed under a Creative Commons Attribution-NonCommercial 3.0 Unported Licence.

Table 3 Isothermal parameters for As(III) adsorption

Materials	TEMP(°C)	Langmuir isotherm			Freundlich isotherm		
		Q_m(mg g^{-1})	K_L	R^2	K_F	$1/n$	R^2
MnO_2/MgFe-LDH	25	53.793	0.0356	0.9846	3.794	0.57684	0.9994
	35	55.843	0.04107	0.9837	4.402	0.5656	0.9991
	45	52.522	0.04839	0.9804	4.985	0.53171	0.9992
MnO_2/MgFe-LDO$_{400\ °C}$	25	51.028	0.06605	0.9765	6.834	0.46887	0.9913
	35	50.360	0.09817	0.9655	9.379	0.41053	0.9904
	45	58.939	0.11574	0.9655	11.785	0.40909	0.9920

Table 4 Comparison of the maximum adsorption capacity of As on LDHs with other adsorbents

Adsorbents	Adsorption capacities (mg g^{-1})	Ref.
MgAl–CO_3-LDH	44.66	Wu *et al.*[41]
MgFeLa-CLDHs	47.40	Jun *et al.*[42]
Mg–Al–Cl	36.00	Pigna *et al.*[43]
Activated carbon	30.50	Rojas *et al.*[44]
HT-Zn-MOF-74	48.70	Mahmoodi *et al.*[45]
UiO-66-$(SH)_2$	40.00	Cox *et al.*[46]
MnO_2/MgFe-LDH	53.79	This study
MnO_2/MgFe-LDO$_{400\ °C}$	51.03	This study

desorption effects of the six adsorbents are shown in Fig. 6(a). The desorption effect of 0.1 mol L^{-1} NaOH was the most superior, with the adsorption capacity can reaching 25.5 and 30.1 mg g^{-1}, respectively. We selected 0.1 mol L^{-1} NaOH as the desorbents to study the regeneration performance of the adsorbent on As(III), and the results are shown in Fig. 6(b). The figure shows that after five times of adsorption–desorption of As(III) by MnO_2/MgFe-LDH and MnO_2/MgFe-LDO$_{400°C}$, the adsorption capacity of the composite still reached 28.5 and 28.9 mg g^{-1}, and the desorption rates were as high as 99% and 96% respectively. This demonstrates that the material can be used repeatedly in treating of As(III), and thus is a renewable and environmentally friendly material that will not cause secondary pollution.

4. Adsorption mechanisms

As shown in Fig. 7(a), before and after the adsorption of As(III) by MnO_2/MgFe-LDH, the peak intensities at 38.087° and 58.722° were weaker than those before adsorption, and the adsorbed material was $AsMn_2O_7$ (ICSD card No.00-042-0035). Combined with the kinetic and isothermal adsorption results, it could be concluded that the adsorption process was chemical-based multilayer adsorption, and it was determined that As(III) and manganese complexed on the surface of the composite material to form a ternary complex to be removed.[47,48] After MnO_2/MgFe-LDO$_{400\ °C}$ adsorbed As(III), the characteristic peaks of $AsMn_2O_7$ (ICSD card No. 00-042-0035) appeared at $2\theta = 20.629°$ (020), 34.118° (220), and 59.096° (003). This demonstrates that manganese participated in the removal reaction of As(III) through surface complexation. In addition, the XRD characteristic peaks of MnO_2/MgFe-LDO$_{400\ °C}$ + As were similar to those of MnO_2/MgFe-LDH, indicating that structural reconstruction of MnO_2/MgFe-LDO$_{400\ °C}$ had occurred due to the "memory effect".[49]

As shown in Fig. 7(b), the tensile vibration absorption peak near 3430 cm^{-1} was obviously enhanced. However, the flexural vibration absorption peak of crystal water between 1632 and 1634 cm^{-1} was still retained after the adsorption As(III) by the two composite materials, indicate that water molecules are absorbed by the adsorbent during the adsorption process. It may also be that As(V) ions have reacted with the hydroxyl

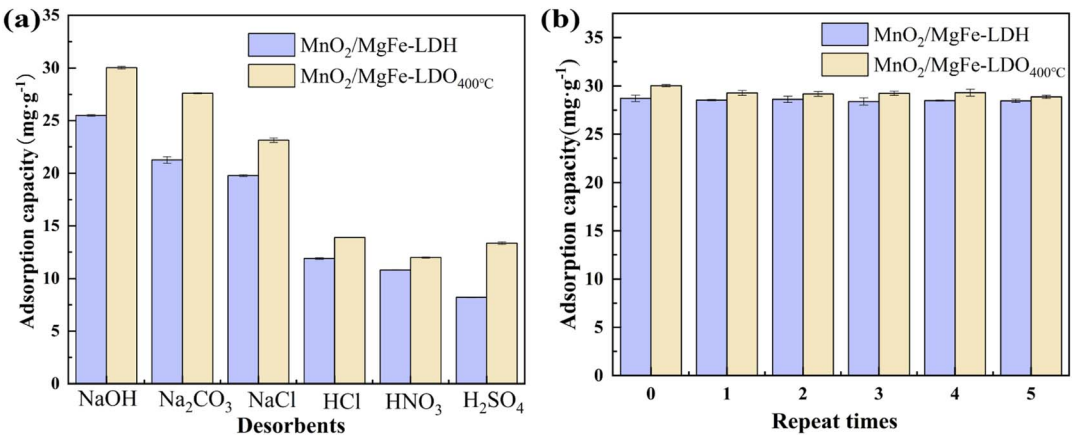

Fig. 6 (a) The influence of six analytical agents on the desorption effect of As(III), (b) the influence of the number of regenerations by the two materials on the adsorption capacity.

Open Access Article. Published on 12 September 2022. Downloaded on 2/12/2026 3:28:12 PM.
This article is licensed under a Creative Commons Attribution-NonCommercial 3.0 Unported Licence.

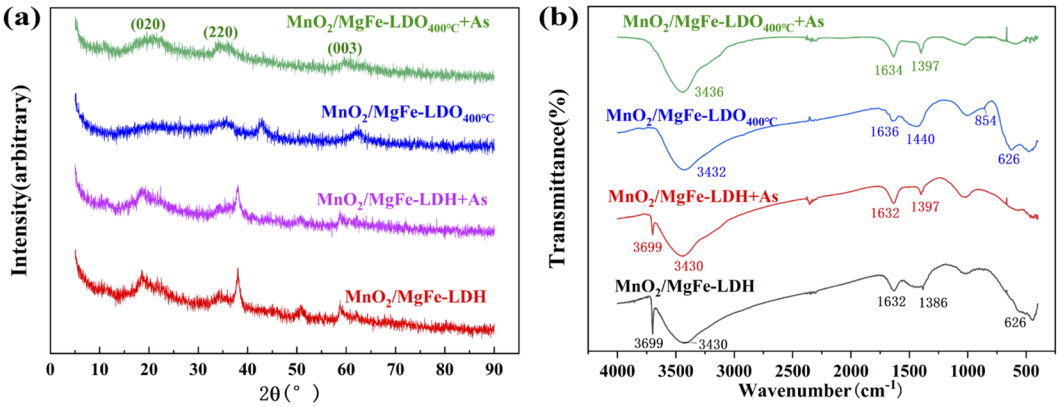

Fig. 7 (a) XRD pattern of MnO_2/MgFe-LDH and MnO_2/MgFe-LDO$_{400\,^\circ C}$ before and after As(III) adsorption. (b) FT-IR of MnO_2/MgFe-LDH and MnO_2/MgFe-LDO$_{400\,^\circ C}$ before and after As(III) adsorption.

groups on the laminate, resulting in interlayer water.[50] The absorption peaks at 626 and 854 cm^{-1} were caused by O-M or O-M-O (M = Mg, Fe, Mn) bending vibrations. After As(III) absorption, the absorption peak intensity weakened or even disappeared. This may be due to the coordination complexation reaction between As(III) and M–O on the laminate material, which produced a number of complexes.[51] The 1386 cm^{-1} peak representing Mn–O shifted to 1397 cm^{-1}, further confirming that Mn–O participated in the reaction. Combined with the adsorption reaction model and XRD analysis, As(III) was partially oxidised to As(V), forming As–O or As–O–As.[52]

The MnO_2/MgFe-LDH and MnO_2/MgFe-LDO$_{400\,^\circ C}$ samples after the As(III) adsorption were analysed for microscopic morphology and elements using SEM-EDS. The results are shown in Fig. 8. The surfaces of the two materials were covered with scale-like substances. Compared with Fig. 3(a–c), after the adsorption of As(III), the surface of the material was rougher, and more granular and scaly substances were present, indicating that new substances of complexes were attached to the material. This can be reciprocally verified with the XRD results.

The surface compositions and valence states of MnO_2/MgFe-LDH and MnO_2/MgFe-LDO$_{400\,^\circ C}$ were analysed by XPS. The high-resolution O 1s spectra are shown in Fig. 9(a). Before the reaction, the O 1s spectra can be deconvoluted into three peaks at approximately 531.1, 531.7, and 532.8 eV, corresponding to the lattice oxygen M–O, –OH and adsorbed-water, respectively. However, after the reaction, the content of the –OH decreased, and a new peak appeared at 531.2 eV, which can be assigned to As–O.[53] It can be concluded that arsenic species achieved the complexation of –OH on the adsorbent surface. Fig. 9(b) shows the As 3d spectra after adsorption of arsenic, indicating that the adsorbed inorganic arsenic species for the two adsorbents were almost As(V) after the reaction.[54] Compared to MnO_2/MgFe-LDH, the As 3d signal of MnO_2/MgFe-LDO$_{400\,^\circ C}$ after adsorption was stronger than that of MnO_2/MgFe-LDH. Therefore, it can be inferred that MnO_2/MgFe-LDO$_{400\,^\circ C}$ favoured the uptake of the arsenic to form As–O-M species.[23,55] As shown in Fig. 9(c–d), for MnO_2/MgFe-LDH before the reaction, the peaks of Mn $2p_{3/2}$ located at 643.81 eV and 642.09 eV were ascribed to Mn(IV) (50.62%) and Mn(II) (49.38%), respectively. After the reaction, the relative proportion of Mn(II) increased from 49.38% to 57%. For MnO_2/MgFe-LDO$_{400\,^\circ C}$, the relative proportion of Mn(II) increased from 51% to 53%. These results suggest the reduction of Mn(IV) to Mn(II), indicating that Mn(IV) participates in electron transfer.

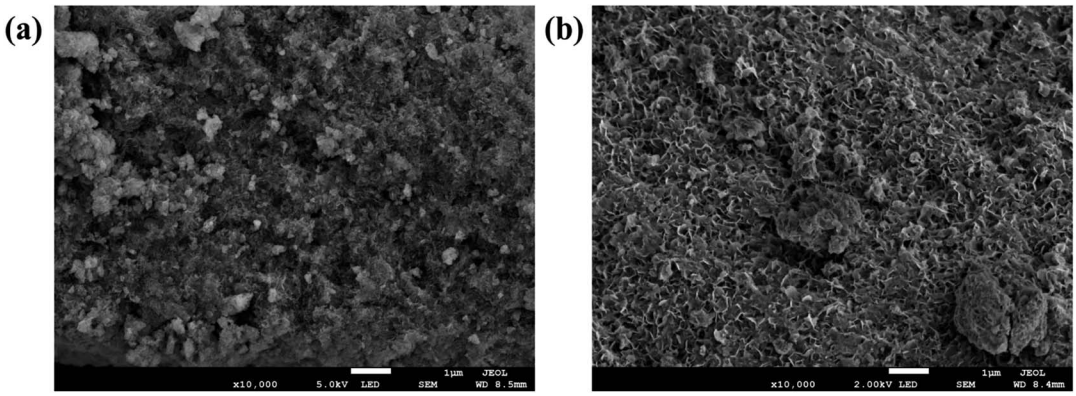

Fig. 8 The SEM images of (a) MnO_2/MgFe-LDH and (b) MnO_2/MgFe-LDO$_{400\,^\circ C}$ after As(III) adsorption.

 © 2022 The Author(s). Published by the Royal Society of Chemistry

Open Access Article. Published on 12 September 2022. Downloaded on 2/12/2026 3:28:12 PM.
This article is licensed under a Creative Commons Attribution-NonCommercial 3.0 Unported Licence.

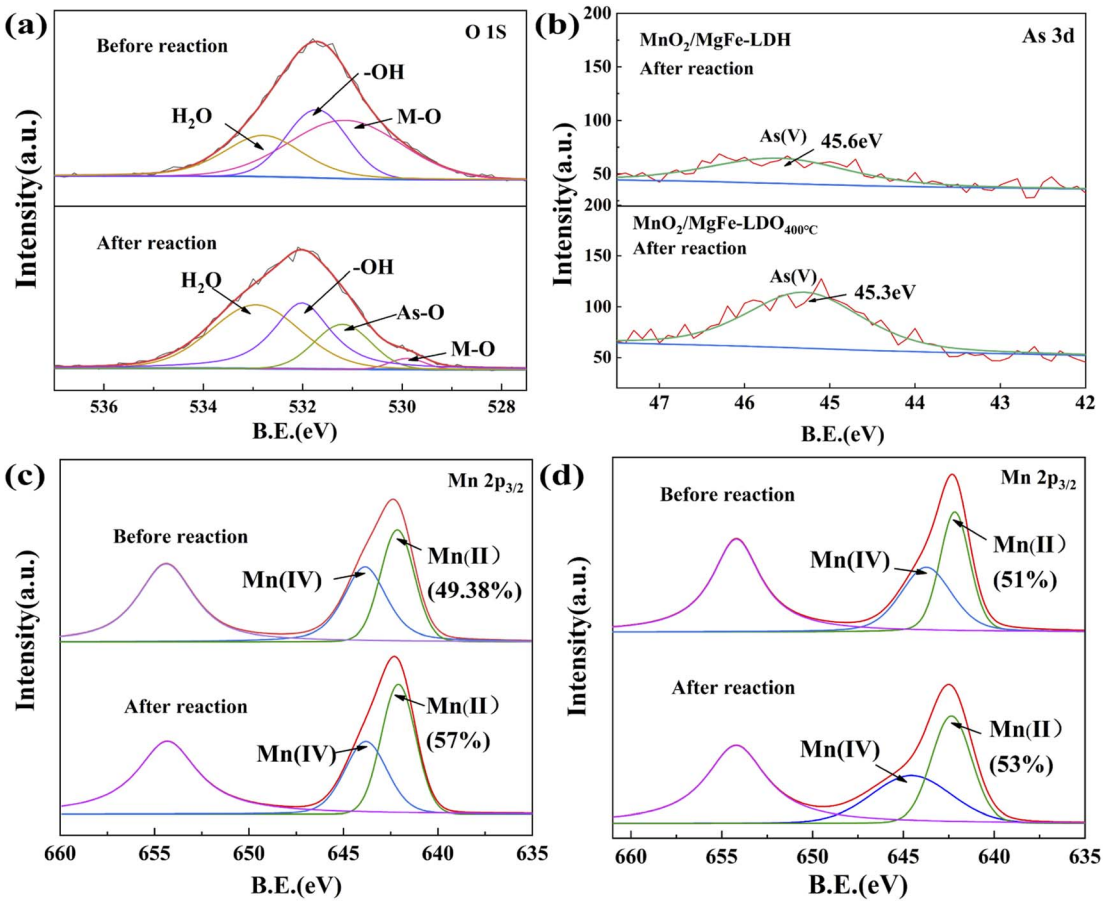

Fig. 9 XPS spectrum of (a) O 1s of MnO_2/MgFe-LDH before and after reaction, (b) As 3d fitting and (c) Mn 2p of MnO_2/MgFe-LDH and (d) MnO_2/MgFe-$LDO_{400\ ^\circ C}$ after As(III) adsorption.

In summary, the main adsorption mechanisms for As(III) removal for MnO_2/MgFe-LDH and MnO_2/MgFe-$LDO_{400\ ^\circ C}$ including complexation, oxidation, and electrostatic attraction, as shown in Fig. 10. The results of XRD, FT-IR, and SEM indicated that As(III) might combine with functional groups of Mn–O or Fe–O on the surface of MnO_2/MgFe-LDH and MnO_2/MgFe-$LDO_{400\ ^\circ C}$ to form complexes, shown in Fig. 10(a). Inner-sphere bidentate surface complex with iron ions on the hydroxide material surface can be formed from $H_2AsO_3^-$ and $H_2AsO_4^-$.[38,56] As shown in Fig. 10(b), some AsO_2^- and H_3AsO_3 were oxidised to $H_2AsO_4^-$ by MnO_2, and MnO_2 mainly acted as an oxidant for oxidation.[57] According to the XPS analysis, electron transfer occurs during adsorption, and the valence states of manganese and arsenic are changed. In addition, the pH adsorption experiment proved the electrostatic attraction between the sorbents and As(III)/As(V) (Fig. 10(c)). At pH < 4.95, the electrostatic attraction was present between the positively charged MnO_2/MgFe-LDH and negatively charged AsO_3^{3-}/AsO_4^{3-}

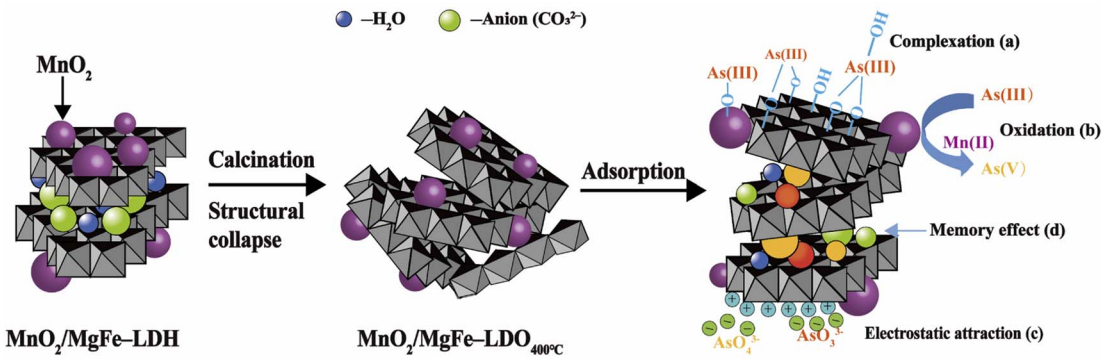

Fig. 10 The As adsorption mechanism of MnO_2/MgFe-LDH and MnO_2/MgFe-$LDO_{400\ ^\circ C}$.

Open Access Article. Published on 12 September 2022. Downloaded on 2/12/2026 3:28:12 PM.
This article is licensed under a Creative Commons Attribution-NonCommercial 3.0 Unported Licence.

(Fig. 4(a)).[39] Similarly, for MnO_2/MgFe-LDO$_{400\ ^\circ C}$, electrostatic attraction could occur in the arsenic removal process when the solution pH was below 5.40. Besides, As(III) also can be absorbed through the "memory effect" of MnO_2/MgFe-LDO$_{400^\circ C}$ (Fig. 10(d)).

5. Conclusion

In summary, the focus of this study was to investigate the adsorption behaviour and preliminary mechanism of heavy metal arsenic in water using two materials MnO_2/MgFe-LDH and MnO_2/MgFe-LDO$_{400\ ^\circ C}$. According to the XRD, FT-IR spectrum, XPS, and SEM-EDS characterisation results, the mechanism of MnO_2/MgFe-LDH and MnO_2/MgFe-LDO$_{400\ ^\circ C}$ mediated adsorption of As(III) was inferred. The adsorption mechanisms of MnO_2/MgFe-LDH and MnO_2/MgFe-LDO$_{400\ ^\circ C}$ adsorbents for As(III) were mainly involved complexation, oxidation, electrostatic attraction, and "memory effect". After the materials adsorbed As(III), it was adsorbed and desorbed by 0.1 mol L^{-1} NaOH for five times, with no significant loss of As(III) adsorption capacity. Therefore, MnO_2/MgFe-LDH and MnO_2/MgFe-LDO$_{400\ ^\circ C}$ composite materials are potential renewable adsorption materials that can effectively adsorb As(III) in water.

Conflicts of interest

The authors declare that they have no known competing financial interests or personal relationships that could have appeared to influence the work reported in this paper.

Acknowledgements

This research was funded by the Science & Technology Program of Guangxi (Grant No. Guike AD19110007, Guike AD19110105 and Guike AD19245065), the Research funds of The Guangxi Key Laboratory of Theory and Technology for Environmental Pollution Control (Grant No. Guikeneng 1801K010), Research Foundation of Guilin University of Technology (Grant No. GUTQDJJ201808), GuangDong Basic and Applied Basic Research Foundation (Grant No. 2021A1515012207).

References

1 Z. Li, D. Zhang, X. Xiong, B. Yan, W. Xie, J. Sheen and J. F. Li, *Nat. Plants*, 2017, **3**, 930–936.
2 P. K. Sahoo and K. Kim, *Geosci. J.*, 2013, **17**, 107–122.
3 M. Jaishankar, T. Tseten, N. Anbalagan, B. B. Mathew and K. N. Beeregowda, *Interdiscip. Toxicol*, 2014, **7**, 60–72.
4 D. Mohan and C. U. Pittman, *J. Hazard. Mater.*, 2007, **142**, 1–53.
5 H. Ba Su, R. K. Singhal, M. V. Pimple and A. Reddy, *Water, Air, Soil Pollut.*, 2015, **226**, 22.
6 D. Lievremont, P. N. Bertin and M. C. Lett, *Biochimie*, 2009, **91**, 1229–1237.
7 T. Yuan, Q. F. Luo, J.-Y. Hu, S.-L. Ong and W. J. Ng, *J. Environ. Sci. Health, Part A: Toxic/Hazard. Subst. Environ. Eng. Part A*, 2003, **38**, 1731–1744.
8 F. Peng, T. Luo and Y. Yuan, *New J. Chem.*, 2014, **38**, 4427–4433.
9 T. F. Lin and J. K. Wu, *Water Res.*, 2001, **35**, 2049–2057.
10 X. J. Gong, Y. S. Li, Y. Q. Dong and W. G. Li, *Chemosphere*, 2020, **250**, 126275.
11 R. Amen, H. Bashir, I. Bibi, S. M. Shaheen, N. K. Niazi, M. Shahid, M. M. Hussain, V. Antoniadis, M. B. Shakoor, S. G. Al-Solaimani, H. Wang, J. Bundschuh and J. Rinklebe, *Chem. Eng. J.*, 2020, **396**, 125195.
12 C. M. Iesan, C. Capat, F. Ruta and I. Udrea, *Water Res.*, 2008, **42**, 4327–4333.
13 P. Hu, S. Wang and Y. Zhuo, *Chem. Eng. J.*, 2022, **431**, 134204.
14 X. Cai, Y. Li, J. Guo, S. Liu and P. Na, *Chem. Eng. J.*, 2014, **248**, 9–17.
15 R. Shabnam, M. A. Rahman, M. A. J. Miah, M. K. Sharafat, H. M. T. Islam, M. A. Gafur and H. Ahmad, *Ind. Eng. Chem. Res.*, 2017, **56**, 7747–7756.
16 J. H. Park, I. Jang, K. Song and S. G. Oh, *J. Phys. Chem. Solids*, 2013, **74**, 1056–1062.
17 M. Li, S. Kuang, Y. Kang, H. Ma, J. Dong and Z. Guo, *Sci. Total Environ.*, 2022, **819**, 153157.
18 Z. Wei, Z. Wang, J. Yan, Y. Liu, Y. Wu, Y. Fang, L. Yu, G. Cheng, Z. Pan and G. Hu, *J. Hazard. Mater.*, 2019, **373**, 232–242.
19 M. Jian, H. Wang, R. Liu, J. Qu, H. Wang and X. Zhang, *Environ. Sci.: Nano*, 2016, **3**, 1186–1194.
20 S. Panimalar, S. Logambal, R. Thambidurai, C. Inmozhi, R. Uthrakumar, A. Muthukumaran, R. A. Rasheed, M. K. Gatasheh, A. Raja, J. Kennedy and K. Kaviyarasu, *Environ. Res.*, 2022, **205**, 112560.
21 L. M. Camacho, R. R. Parra and S. Deng, *J. Hazard. Mater.*, 2011, **189**, 286–293.
22 J. Li, H. Yu, T. Yan, M. Sun, X. Li, W. Song and L. Yan, *Colloids Surf., A*, 2022, **634**, 128021.
23 C. Ye, J. Deng, L. Huai, A. Cai, X. Ling, H. Guo, Q. Wang and X. Li, *Sci. Total Environ.*, 2022, **806**, 150379.
24 X. Feng, R. Long, L. Wang, C. Liu, Z. Bai and X. Liu, *Sep. Purif. Technol.*, 2022, **284**, 120099.
25 X. Dai, W. Yi, C. Yin, K. Li, L. Feng, Q. Zhou, Z. Yi, X. Zhang, Y. Wang, Y. Yu, X. Han and Y. Zhang, *Appl. Clay Sci.*, 2022, **229**, 106664.
26 F. L. Long, C. G. Niu, N. Tang, H. Guo, Z. W. Li, Y. Y. Yang and L. S. Lin, *Chem. Eng. J.*, 2021, **404**, 127084.
27 Z. Lv, S. Yang, H. Zhu, L. Chen, N. S. Alharbi, M. Wakeel, A. Wahid and C. Chen, *Appl. Surf. Sci.*, 2018, **448**, 599–608.
28 M. Mubarak, H. Jeon, M. S. Islam, C. Yoon, J. S. Bae, S. J. Hwang, W. S. Choi and H. J. Lee, *Chemosphere*, 2018, **201**, 676–686.
29 Y. S. Ho and G. McKay, *Chem. Eng. J.*, 1998, **70**, 115–124.
30 B. Zhou, Y. Wu, J. Chan, S. Wang and S. Hu, *Bull. Environ. Contam. Toxicol.*, 2019, **103**, 75–81.
31 F. Cheng, H. Guo, J. Cui, B. Hou, H. Xi, L. Jia and D. Li, *Reaction Kinetics, Mechanisms and Catalysis*, 2019, **126**, 119–136.
32 J. Zhang, F. Zhang, L. Ren, D. G. Evans and X. Duan, *Mater. Chem. Phys.*, 2004, **85**, 207–214.

 © 2022 The Author(s). Published by the Royal Society of Chemistry

Open Access Article. Published on 12 September 2022. Downloaded on 2/12/2026 3:28:12 PM.
This article is licensed under a Creative Commons Attribution-NonCommercial 3.0 Unported Licence.

33 P. x. Wu, W. Li, Y.-j. Zhu, Y. n. Tang, N. w. Zhu and C. l. Guo, *Appl. Clay Sci.*, 2014, **100**, 76–83.
34 I. Lagadic, A. Léaustic and R. Clément, *J. Chem. Soc., Chem. Commun.*, 1992, **19**, 1396–1397.
35 M. K. Titulaer, J. B. H. Jansen and J. W. Geus, *Clays Clay Miner.*, 1994, **42**, 249–258.
36 M. T. Hasan, B. J. Senger, C. Ryan, M. Culp, R. Gonzalez-Rodriguez, J. L. Coffer and A. V. Naumov, *Sci. Rep.*, 2017, **7**, 6411.
37 H. Fu, Z. j. Du, W. Zou, H. q. Li and C. Zhang, *Carbon*, 2013, **65**, 112–123.
38 P. K. Raul, R. R. Devi, I. M. Umlong, A. J. Thakur, S. Banerjee and V. Veer, *Mater. Res. Bull.*, 2014, **49**, 360–368.
39 Y. Y. Wang, H.-Y. Ji, H. H. Lu, Y. X. Liu, R. Q. Yang, L. L. He and S. M. Yang, *RSC Adv.*, 2018, **8**, 3264–3273.
40 M. F. Torres, J. M. González, M. R. Rojas, A. J. Müller, A. E. Sáez, D. Löf and K. Schillén, *J. Colloid Interface Sci.*, 2007, **307**, 221–228.
41 X. Wu, X. Tan, S. Yang, T. Wen, H. Guo, X. Wang and A. Xu, *Water Res.*, 2013, **47**, 4159–4168.
42 H. Jun, Z. Zhiliang, L. Hongtao and Q. Yanling, *RSC Adv.*, 2014, **4**, 5156–5164.
43 M. Pigna, J. J. Dynes, A. Violante, A. Sommella and A. G. Caporale, *Environ. Eng. Sci.*, 2015, **33**, 98–104.
44 S. Rojas and P. Horcajada, *Chem. Soc. Rev.*, 2020, **120**, 8378–8415.
45 N. M. Mahmoodi, M. Oveisi, A. Taghizadeh and M. Taghizadeh, *J. Hazard. Mater.*, 2019, **368**, 746–759.
46 C. S. Cox, V. Cossich Galicia and M. Lessio, *J. Phys. Chem. C*, 2021, **125**, 3157–3168.
47 J. Wu, D. Huang, X. Liu, J. Meng, C. Tang and J. Xu, *J. Hazard. Mater.*, 2018, **348**, 10–19.
48 S. Hu, L. Yan, T. Chan and C. Jing, *Environ. Sci. Technol.*, 2015, **49**, 5973–5979.
49 C. T. Vu and T. Wu, *Water Res.*, 2020, **175**, 115679.
50 W. Xu, J. Wang, L. Wang, G. Sheng, J. Liu, H. Yu and X. J. Huang, *J. Hazard. Mater.*, 2013, **260**, 498–507.
51 R. Dou, J. Ma, D. Huang, C. Fan, W. Zhao, M. Peng and S. Komarneni, *Appl. Clay Sci.*, 2018, **161**, 235–241.
52 X. Ge, J. Liu, X. Song, G. Wang, H. Zhang, Y. Zhang and H. Zhao, *Chem. Eng. J.*, 2016, **301**, 139–148.
53 B. Hudcová, V. Veselská, J. Filip, S. Číhalová and M. Komárek, *Chemosphere*, 2017, **168**, 539–548.
54 D. Kang, X. Yu, S. Tong, M. Ge, J. Zuo, C. Cao and W. Song, *Chem. Eng. J.*, 2013, **228**, 731–740.
55 S. Ploychompoo, J. Chen, H. Luo and Q. Liang, *J. Environ. Sci.*, 2020, **91**, 22–34.
56 P. R. Grossl, M. Eick, D. L. Sparks, S. Goldberg and C. C. Ainsworth, *Sci. Technol.*, 1997, **31**, 321–326.
57 Q. Zheng, J. Hou, W. Hartley, L. Ren, M. Wang, S. Tu and W. Tan, *Chem. Eng. J.*, 2020, **389**, 124470.